

DIRECT IMAGING OF THE CMB FROM SPACE

Michael A. Janssen¹, Douglas Scott², Martin White³, Michael D. Seiffert⁴, Charles R. Lawrence¹, Krzysztof M. Górska⁵, Mark Dragovan³, Todd Gaier⁴, Ken Ganga⁶, Samuel Gulkis⁷ Andrew E. Lange⁶, Steven M. Levin¹, Philip M. Lubin⁴, Peter Meinhold⁴, Anthony C. S. Readhead⁸, Paul L. Richards⁹, & John E. Ruhl⁴

ABSTRACT

Vast amounts of information about the Universe are encoded in anisotropies of the Cosmic Microwave Background (CMB). An experiment designed to fully exploit this information must image the entire sky with the angular resolution, sensitivity, and spectral coverage necessary to reach the fundamental limits set by cosmic variance on angular scales $\gtrsim 10'$. Recent advances in detector technology enable this limit to be achieved by a properly designed space mission that fits well within the scope of NASA's Medium-class Explorer program. An essential component of the mission design is an observing strategy that minimizes systematic effects due to instrumental offset drifts. Recent advances in detectors enable a "spin-chopping" strategy that has significant technical and scientific advantages over the strategy used by COBE, which reconstructed an image of the sky via inversion of a large matrix of differential measurements. These advantages include increased angular resolution, increased sensitivity, and simplicity of instrumentation and spacecraft operations. For the parameters typical of experiments like the Primordial Structures Investigation (PSI) and the Far InfraRed Explorer (FIRE), we show that the spin-chopping strategy produces images of the sky and power spectra of CMB anisotropies that contain no significant systematic artifacts.

Subject headings: cosmic microwave background—space vehicles—methods: observational—methods: data analysis

Submitted to – *The Astrophysical Journal*

¹ Astrophysics 169-506, Jet Propulsion Laboratory, 4800 Oak Grove Drive, Pasadena, CA 91109

² Department of Geophysics & Astronomy 129-2219 Main Mall, University of British Columbia, Vancouver, B.C. V6T 1Z4 Canada

³ Enrico Fermi Institute, 5640 S. Ellis Avenue, Chicago IL 60637

⁴ Department of Physics, University of California, Santa Barbara, CA 93106

⁵ Code 685, NASA Goddard Space Flight Center, Greenbelt, MD 20771, on leave from Warsaw University Observatory, Poland

⁶ Observational Cosmology 59-33, California Inst. of Tech., Pasadena, CA 91125

⁷ MS 180-703, Jet Propulsion Laboratory, 4800 Oak Grove Drive, Pasadena, CA 91109

⁸ Astronomy 105-24, California Inst. of Tech., Pasadena, CA 91125

⁹ Department of Physics, University of California, Berkeley, CA 94720

1 INTRODUCTION

The study of the Cosmic Microwave Background (CMB) entered an exciting new phase with the detection of large scale anisotropies by the *COBE*-DMR (Smoot et al. 1992). Degree-scale fluctuations have now been detected by several ground- and balloon-based experiments (Cheng et al. 1995; de Bernardis et al. 1994; Ganga et al. 1994; Gundersen et al. 1995; Hancock et al. 1994; Netterfield et al. 1995; Piccirillo et al. 1996; Ruhl et al. 1995; Tanaka et al. 1996). Full realization of the enormous scientific potential of the CMB, however, will require a high-sensitivity, high-angular-resolution study of a large fraction of the sky from a single, stable platform. Due to dramatic advances in detector sensitivity and stability over the last decade, such a study is now feasible, and several groups have devoted substantial effort to developing plans for a second-generation space experiment capable of extracting the maximum available cosmological information from the CMB.

An important element in the design of a CMB experiment is the scan strategy, which in addition to specifying how different parts of the sky are observed must provide extremely good control of potential sources of systematic errors. The aforementioned advances in detector technology coupled with recent advances in mission design allow a direct-imaging strategy that has been adopted by two proposed space missions: the Primordial Structures Investigation (PSI) and the Far-InfraRed Explorer (FIRE). This strategy has many advantages over the differential chopping scheme used by *COBE*-DMR. The main subject of this paper is the demonstration, through analytical calculations and simulations, that this direct-imaging strategy can produce images of the sky containing no significant systematic artifacts, especially those due to instrumental fluctuations with a $1/f$ spectrum. We begin by introducing the scan strategy and its advantages.

PSI and FIRE each propose to use a spinning spacecraft located near the Earth-Sun L_2 point, with the spin axis pointed at the Sun and the boresight of a single telescope at right angles to the spin axis. The individual beams of a focal plane array of detectors sweep out great circles through the ecliptic poles. The spin axis is precessed either in small steps (6.67 nine times daily for PSI) or continuously (FIRE) to maintain Sun-pointing. The output of the detectors is sampled rapidly ($\gtrsim 3.5$ times per beam) around each circle. An image of the whole sky is built up steadily over 6 months as the Earth and the spacecraft orbit the Sun. Since each great circle is scanned many times in succession, instrumental drifts or offsets on timescales long compared to the spin period are easily removed. The north and south ecliptic pole regions tie any given great circle to all others.

In contrast, the differential chopping scheme used by *COBE*-DMR (Boggess et al. 1992) measures differences in power between two horn antennas or telescopes pointed at widely-separated positions on the sky. The horns spin around a bisecting axis, which itself is steered around the sky at a slower rate. After essentially the entire sky has been scanned the image is constructed by inverting a large matrix of temperature differences (Janssen & Gulkis 1992). The differential chopping strategy reduces the effects of gain drifts in detectors as well as time-varying instrumental or atmospheric offsets, but at the price of decreased sensitivity and increased complexity of instrumentation and observing strategy. Historically this approach has been required when stability could be achieved in no other way. A variant of this strategy has been chosen for the Microwave Anisotropy Probe (MAP: Wright, Hinshaw, & Bennett 1995), another proposed second-generation CMB mission.

The spin-chopping strategy used by PSI and FIRE has many advantages, either by itself or as an enabling factor in the mission design. A complete discussion of these advantages would require full specifications of the spacecraft and mission designs, which are beyond the scope of the paper, but we introduce sufficient detail here to motivate the discussion that follows. The main advantages are:

- (1) Simplicity of the hardware. Only a single telescope is required, and the complications of internal switches or correlation receivers are avoided.
- (2) Superior angular resolution. A single-telescope design allows the largest possible aperture within the size limitations of the launch vehicle. Detailed theoretical investigation of CMB anisotropies shows unequivocally that even modest increases in angular resolution in the critical sub-degree region can have dramatic scientific benefits.
- (3) Increased sensitivity. The low instrument temperatures that can be achieved passively with the Sun-pointed spin axis (next item) lead directly or indirectly to colder and more sensitive detectors. Moreover, an unswitched system has a factor of $\sqrt{2}$ greater sensitivity than a switched system that differences pairs of pixels on the sky (Janssen & Gulkis, 1992).
- (4) Extremely benign and stable thermal conditions. With the spin axis pointed at the Sun (and $< 5^\circ$ from the Earth) the drivers for spin-synchronous temperature changes are essentially eliminated. A solar panel at one end of the spacecraft normal to the spin axis shades the rest of the spacecraft from the Sun and Earth at all times. Passive cooling of the instrument end of the spacecraft to below 60 K is readily achieved.
- (5) A direct image of the sky is formed incrementally as it is observed. One does not have to wait until a large fraction of the sky (for *COBE*-DMR almost the entire sky) is observed to form an image. This significantly reduces the science risk of an early mission failure, and allows immediate investigation of mission performance and potential systematic errors at the microkelvin level.
- (6) It gives a direct measure of $1/f$ noise in the instrument, since each great circle is “closed.” The differential strategy is vulnerable to drifts in the switched system offset. While this was relatively easy to handle in *COBE*-DMR, the problem becomes more severe at higher angular resolutions and sensitivities where the beams are not swapped precisely on the sky in the measurement of each pixel pair. Also, thermal gradients are more difficult to control with two large telescopes than with two small horns.
- (7) Data from different parts of the sky are independent. There is no aliasing of signal from high foreground regions such as the Galactic plane into foreground-free regions as there may be in differential chopping schemes (see also Lineweaver et al. 1994). Similarly, the effects of transients, either in the instrument or on the sky (e.g., variable or moving sources such as planets) are localized, and the large number of scans over a given great circle provides many cross-checks on a pixel-by-pixel basis.
- (8) Simplicity of spacecraft operations. The almost stationary spin axis simplifies attitude control and ground communications.

These advantages would be lost if medium-timescale instrumental fluctuations that could not be “chopped out” by the spacecraft spin introduced serious systematic errors. Such fluctuations might be caused by, for example, detector gain variations or temperature changes in the optical system with a $1/f$ spectrum. Naively one might expect that the detectors would have to have essentially no such fluctuations on timescales shorter than the spin period. In this paper we derive analytical expressions for the effect of $1/f$ noise on sky images obtained with the scan strategy described. We also verify the analytical results with simulations of sky images at very high resolution, using detector characteristics measured in the laboratory for both transistor amplifiers (for PSI) and bolometers (for FIRE). We show that the naive expectation that detector fluctuations must be on timescales longer than the spin period is far too restrictive, and that a spin-chopping mission in the benign L_2 environment with recently developed and characterized transistor amplifiers or bolometers can realize all of the above advantages.

2 THEORETICAL ANALYSIS

The spacecraft spin acts as an ideal switch or chop to suppress slowly varying drifts and offsets; however, the effects of instrumental drifts on timescales less than the spin period cannot be suppressed completely by the spin. In an instrument based on either indium phosphide high-electron-mobility transistor amplifiers (PSI) or AC-biased bolometers operated from a temperature regulated heat sink (FIRE), these drifts are measured to have a $1/f$ spectrum dominated by transistor gain fluctuations.

In this section we derive analytic expressions for the effect of such drifts on an image of the sky on a single scan circle (combining different scan circles is discussed in the next section). The main effect turns out to be an increase in the rms noise in the image that depends on the spacecraft spin rate and on the frequency at which the $1/f$ and the “white” noise have the same amplitude, known as the $1/f$ knee frequency.

Assume a time-varying signal $T(t)$ due to stationary noise that is characterized by the noise power spectrum $S(f)$, where f is frequency. The signal is measured as a uniform series of contiguous averages over integration time Δt ,

$$T_i = \int_{t_0+(i-1)\Delta t}^{t_0+i\Delta t} T(t) dt, \quad (1)$$

where t_0 is some arbitrary reference time. We wish to determine the variance

$$\sigma^2(j - k) = \frac{1}{2} \langle (T_j - T_k)^2 \rangle \quad (2)$$

in terms of the time-lag index $j - k$, the integration time Δt , and the noise power spectrum $S(f)$. Angle brackets denote ensemble averages. Defining $n \equiv j - k$ and using the stationarity property of the noise, this equation may be rewritten as

$$\sigma^2(n) = \langle T_j^2 \rangle - \langle T_j T_k \rangle. \quad (3)$$

Using Eqn. (1) and

$$\langle T(t)T(t - \tau) \rangle = \int_0^\infty S(f) \cos(2\pi f\tau) df, \quad (4)$$

we find

$$\sigma^2(n) = \frac{2}{\Delta t^2} \int_0^\infty S(f) \frac{\sin^2(\pi f \Delta t)}{(\pi f)^2} \sin^2(n\pi f \Delta t) df. \quad (5)$$

We have measured the detected-power spectrum $S(f)$ of the InP HEMT amplifiers and bolometers that will be used by PSI (Seiffert et al. 1996; Gaier et al. 1996b) and FIRE, respectively. For both, S is well-represented by

$$S(f) = a + b/f \quad (6)$$

for which Eqn. (5) becomes

$$\sigma^2(n) = \frac{a}{2\Delta t} \left[1 + \frac{b}{a} \Delta t \phi(n) \right], \quad (7)$$

where

$$\begin{aligned} \phi(n) &= (n-1)^2 \ln(n-1) - 2n^2 \ln n + (n+1)^2 \ln(n+1) \\ &\rightarrow 2 \ln n + 3 \quad \text{as } n \rightarrow \infty. \end{aligned} \quad (8)$$

(Convergence is rapid. For $n \geq 10$ the error is $\leq 10^{-3}$.) The logarithmic behavior of ϕ , essential in what follows, is illustrated in Figure 1. Note that the noise characteristics of many detectors *cannot* be represented by Eq. (6). For example, the detectors used on IRAS exhibited strong memory effects, which introduced large offsets whenever a bright object was crossed. Such detectors would be quite unsuitable for spin-chopped observations of the CMB.

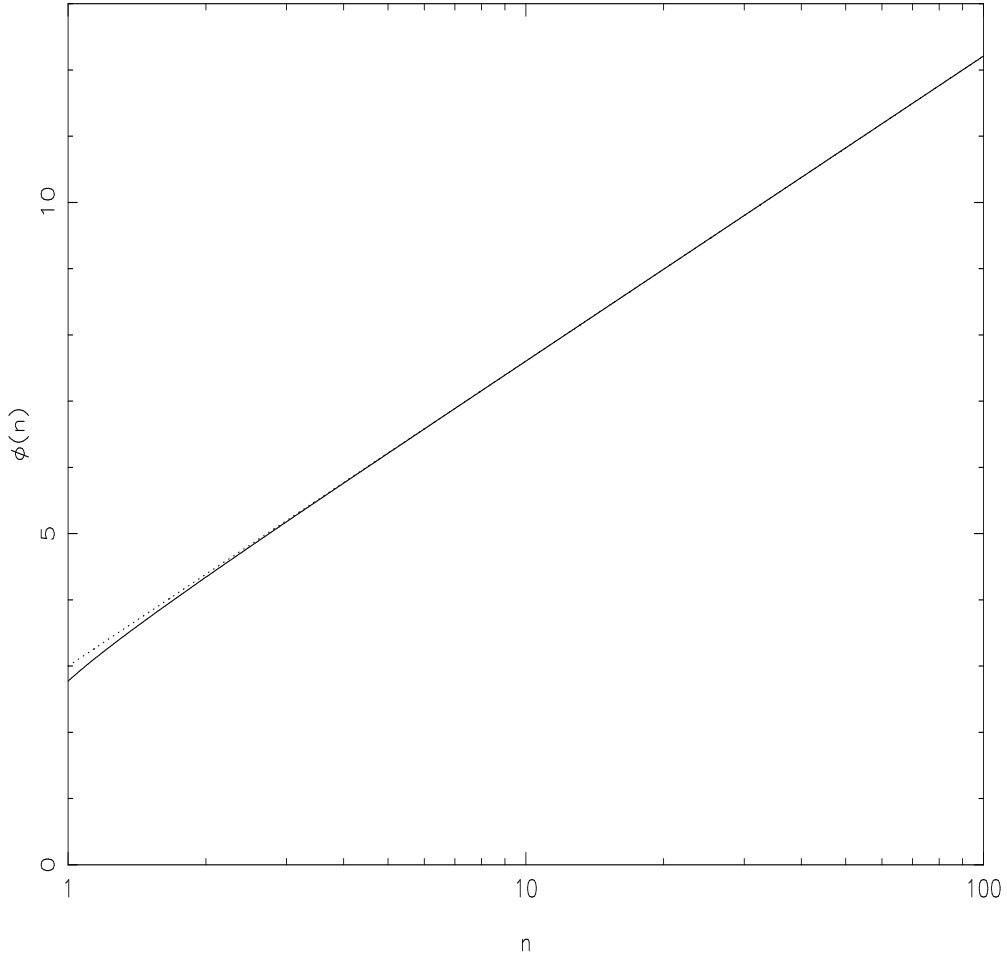


Fig. 1 $\phi(n)$ from Eqn. (8). The dotted line shows the approximation $\phi = 2 \ln n + 3$, which gives an error $\leq 10^{-3}$ for $n \geq 10$.

The variance σ_0^2 for a total power radiometer with pure white noise (i.e., $b = 0$ in Eqn. (6)) is well known to be

$$\sigma_0^2 = \frac{T_s^2}{B \Delta t}, \quad (9)$$

where T_s is the system noise temperature, B is the radiometer bandwidth, and Δt is the averaging time for a given sample as defined in Eqn. (1). Eqn. (7) may then be written as

$$\sigma^2(n) = \sigma_0^2 [1 + \Delta t f_{\text{knee}} \phi(n)] \quad (10)$$

where $f_{\text{knee}} \equiv b/a$ is the frequency at which the white noise and $1/f$ noise contributions are equal. The factor

$$F = [1 + \Delta t f_{\text{knee}} \phi(n)]^{1/2} \quad (11)$$

thus gives the increased uncertainty over the case of perfect white noise.

Now consider a scan circle divided into m uniform and contiguous integrations, and assume that the circle is scanned N times and that the N measurements at each pixel are averaged. Specifically, for two pixels $1 \leq p < q \leq m$ around the circle, these averages are

$$\begin{aligned}\overline{T}_p &= \frac{1}{N} \sum_{i=1}^N T_{p+(i-1)m}, \\ \text{and } \overline{T}_q &= \frac{1}{N} \sum_{i=1}^N T_{q+(i-1)m}.\end{aligned}\tag{12}$$

Let us find the variance

$$\sigma^2(n = q - p, m, N) = \frac{1}{2} \langle (\overline{T}_q - \overline{T}_p)^2 \rangle. \tag{13}$$

Substituting Eqn. (12) into (13), expanding, and making use of Eqn. (3), we obtain

$$\sigma^2(n, m, N) = \frac{1}{N} \sigma^2(n) - \frac{1}{N^2} \sum_{k=1}^{N-1} (N - k) \left\{ 2\sigma^2(km) - \sigma^2[km + n] - \sigma^2[km - n] \right\}. \tag{14}$$

Using Eqn. (10), we arrive at

$$\sigma^2(n, m, N) = \frac{\sigma_0^2}{N} \left[1 + \Delta t f_{\text{knee}} \Phi(n, m, N) \right], \tag{15}$$

where

$$\Phi(n, m, N) = \phi(n) - \frac{1}{N} \sum_{k=1}^{N-1} (N - k) \left\{ 2\phi(km) - \phi[km + n] - \phi[km - n] \right\}. \tag{16}$$

The factor

$$F(n, m, N) = \left[1 + \Delta t f_{\text{knee}} \Phi(n, m, N) \right]^{1/2} \tag{17}$$

gives the increase in image uncertainty in the scan-averaged image over the white-noise case. Figure 2 shows $\Phi(n, m, N)$ for typical parameters. The case $N = 1$ consists of only one scan with no scan averaging, so that the factor F increases simply as the two-point variance. As N increases Φ becomes symmetric around the midpoint, reflecting the fact that pixels beyond the midpoint move closer to the first pixel of the next scan, shortening the effective time between pixel pairs. PSI will average 1600 scans before redirecting the spacecraft spin axis, so that we are practically concerned only with the asymptotic form for large N . FIRE will have $N \gg 1$, but much smaller than for PSI. Note that for $N \gtrsim 10$, $\Phi(n, m, N)$ depends hardly at all on N , and $\sigma^2 \propto N^{-1}$.

The uncertainty is a maximum between diametrically opposed pixels if N is large. From the above we may write

$$F_{\text{max}}(m, N) = F(m/2, m, N) = \left[1 + \Delta t f_{\text{knee}} \Phi_{\text{max}}(m, N) \right]^{1/2}, \tag{18}$$

$$\Phi_{\text{max}}(m, N) = \phi(m/2) - \frac{1}{N} \sum_{k=1}^{N-1} (N - k) \left\{ 2\phi(km) - \phi[(k + 1/2)m] - \phi[(k - 1/2)m] \right\}. \tag{19}$$

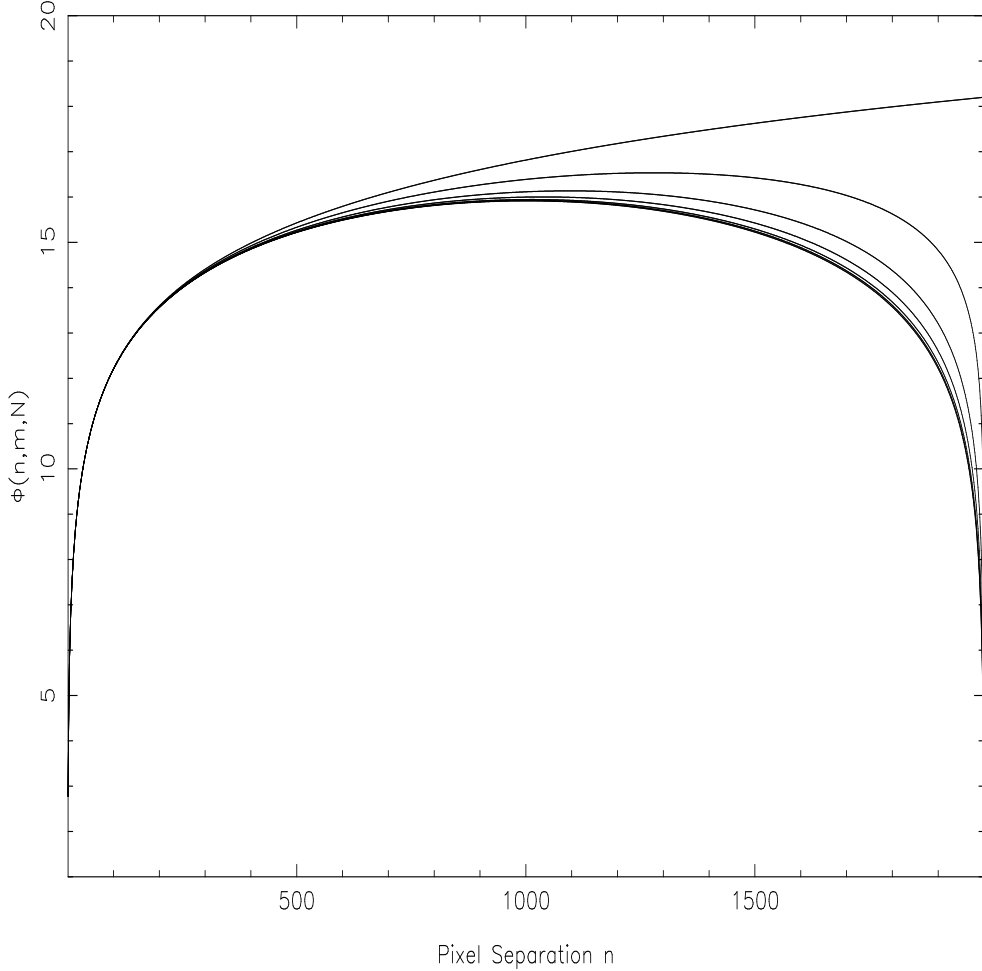


Fig. 2 $\Phi(n, m, N)$ from Eqn. (16) as a function of pixel separation n for a scan circle consisting of $m = 2000$ pixels. Seven curves are plotted, for (top to bottom) $N = 1, 3, 10, 30, 100, 300$, and 1600 . The curves for $N = 300$ and $N = 1600$ are almost indistinguishable. For PSI, $m = 1700$ (corresponding to a 12:6 beam) and $N = 1600$. For FIRE, $m = 2700$ (corresponding to an 8' beam) and $N = 18$. For large m the curves are insensitive to m .

For large N the sum may be approximated as an integral and the term in $\{\dots\}$ is approximately $\phi''(x) \sim x^{-2}$. The sum is thus only logarithmically dependent on m . Numerical evaluation gives 0.871 for $N > 50$ almost independent of m . Hence we can approximate

$$\Phi_{\max}(m) = \lim_{N \rightarrow \infty} \Phi_{\max}(m, N) \simeq \phi(m/2) - 0.871. \quad (20)$$

Further, if $m \gtrsim 10$, we can simplify this to

$$\Phi_{\max}(m) \simeq 2 \ln m + 0.743. \quad (21)$$

The maximum excess noise factor for a typical PSI or FIRE scan circle can therefore be approximated closely as

$$F_{\max} \simeq [1 + \Delta t f_{\text{knee}} (2 \ln m + 0.743)]^{1/2}. \quad (22)$$

F_{\max} is plotted in Figure 3 as a function of f_{knee} for the PSI and FIRE spin rates. Note that the sensitivity of a differential chopping instrument corresponds to $F_{\max} = \sqrt{2}$.

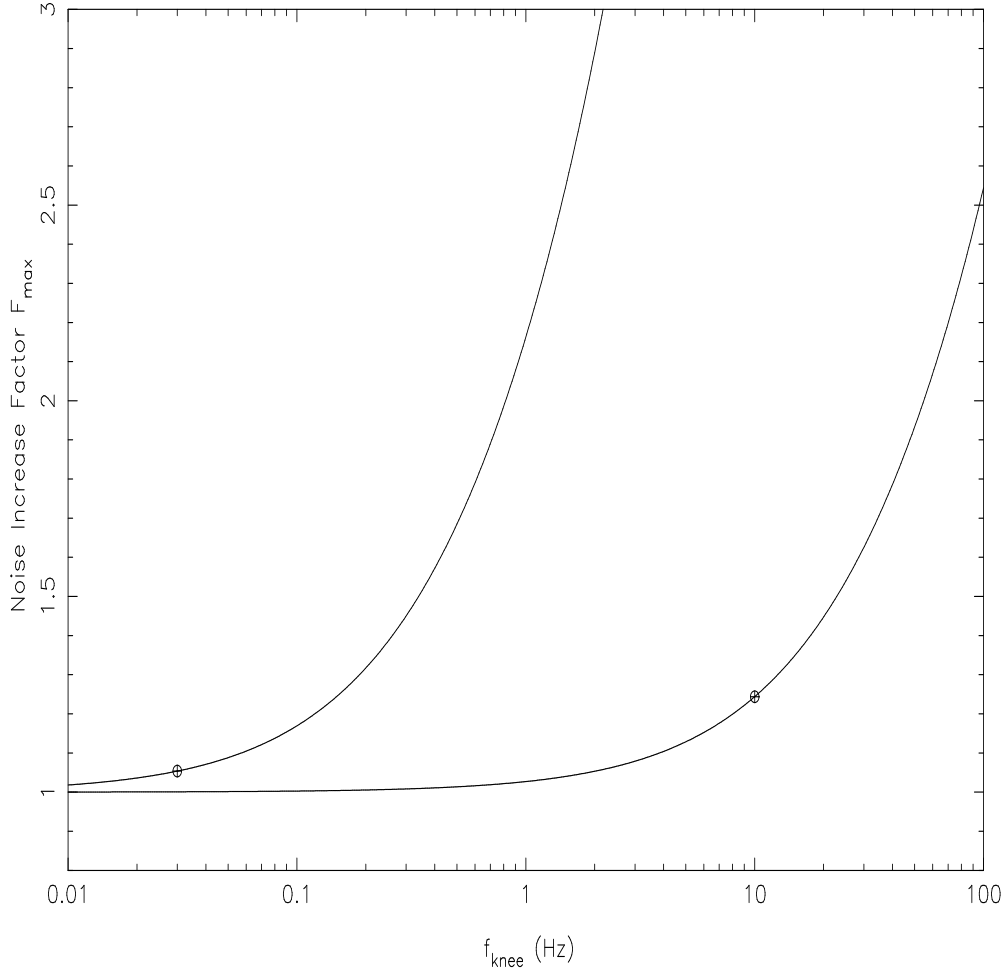


Fig. 3 F_{\max} from Eqn. (22) versus f_{knee} for the PSI and FIRE spin rates of 10 and 0.1 rpm, respectively. The pixel size for the PSI curve (lower) is 12.6', while that for the FIRE curve is 8'. The symbols mark knee frequencies measured in the laboratory for stabilized InP HEMT amplifiers for PSI (10 Hz; Seiffert et al. 1996; Gaier et al. 1996b) and bolometers for FIRE (0.03 Hz).

Based on laboratory measurements, $f_{\text{knee}} \simeq 10$ Hz for the stabilized HEMTs used by PSI (Seiffert et al. 1996; Gaier et al. 1996b), and $f_{\text{knee}} \simeq 0.03$ Hz for the bolometers used by FIRE. These knee frequencies correspond to increases in the noise over the $S(f) = \text{constant}$ (pure white noise) case of only about 24% for PSI and 6% for FIRE. This is significantly less even than the minimum increase of noise in a switching system of $\sqrt{2}$.

3 SIMULATIONS

The foregoing calculation gives the variance between pixels on a given scan circle, which does not depend on the mean value. The variance between pixels on *different* scan circles, however, does depend on the mean values of the two circles. Since we are interested only in CMB anisotropies, the mean level itself is unimportant. On the other hand, since the mean value of a $1/f$ noise component formally diverges as the averaging time increases, the mean levels on different scan circles will in general be different, and if not removed would produce stripes parallel to the scan direction.

Assume for the moment that the offsets between scan circles have been determined and removed. The variance between pixels on the circle is unchanged. The variance between random pixels on *different* circles depends on how accurately the offset was removed and on the relative phases of the dominant $1/f$ fluctuations along the two circles. If we assume that the offset has been subtracted with an error small compared to $\sigma_{\max} \equiv \sigma_0(F_{\max}/N)^{1/2}$, then σ_{\max}^2 should be an upper bound on the variance calculated between random pixels on different circles.

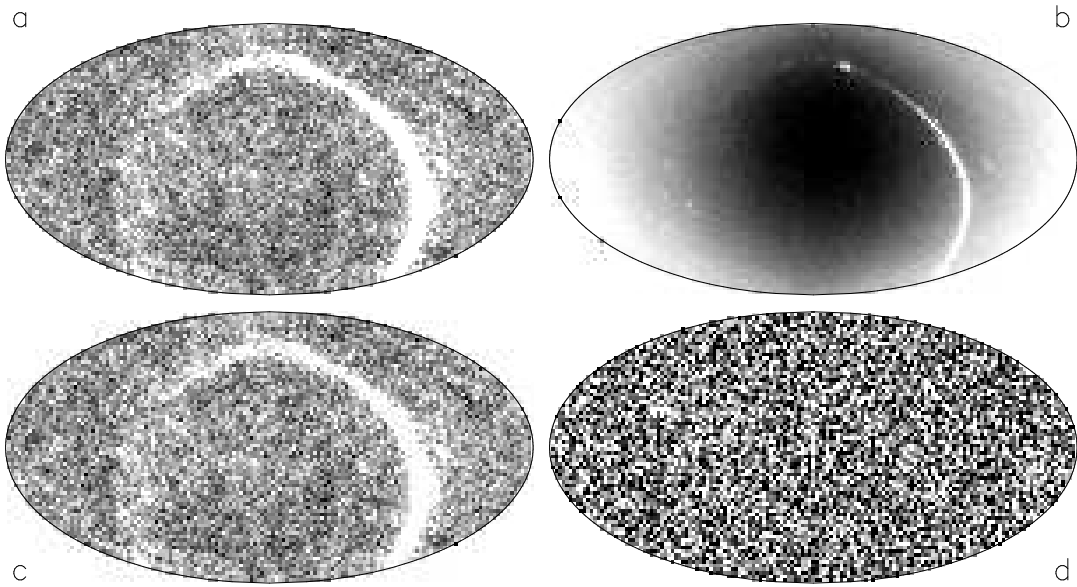


Fig. 4 All-sky PSI simulation at 90 GHz, including both white and $1/f$ noise. The FIRE simulation at a similar frequency is indistinguishable from this one. All images are Aitoff projections in ecliptic coordinates, with $12.6'$ pixels, to match roughly the resolution of the printer. (For a standard printer at 600 dots per inch, this gives 1.25 dots per pixel, and the image is therefore black and white, not grayscale.) **a)** Assumed sky, using a standard CDM model to generate CMB fluctuations together with extrapolations of Galactic data taken at other frequencies. The stretch is $\pm 300 \mu\text{K}$. **b)** Same as before, but including instrument noise (white noise + $1/f$ noise as measured in the laboratory at 90 GHz) and the dipole. The stretch is $\pm 3000 \mu\text{K}$ to accommodate the dipole. **c)** Observed sky, following fitting and removal of the dipole, plus DC-offset and gradient terms in each great circle. The stretch is $\pm 300 \mu\text{K}$. **d)** Difference between lower left and upper left images stretched to $\pm 30 \mu\text{K}$, showing the high SNR achieved. Residual striping is seen along lines of constant longitude at the level expected from the calculations in § 2. Stripes parallel to the sides of the paper are caused by unevenness in the printer, not the experiment! **Note:** the figure above has been drastically reduced in resolution in order to be a manageable 100 k postscript file. Full resolution and colour versions of this figure can be found at <http://astrophysics.jpl.nasa.gov/PSI>.

To complete our demonstration that the spin-chopping strategy leads to no significant systematic errors due to medium-timescale instrumental fluctuations, we now describe simulations of full-sky images that: 1) demonstrate that offsets between scan circles can be removed; 2) verify the conjecture that σ_{\max}^2 is a good estimator of the variance in the full-sky images; and 3) show that there are no significant artifacts of any kind in the images.

We simulated a CMB signal at $< 1'$ resolution assuming a standard Cold Dark Matter (CDM) model with $h = 0.5$, $\Omega_0 = 1$ and $\Omega_B = 0.05$. To this cosmic signal we added Galactic emission extrapolated from IRAS and DIRBE (for the dust) and ground based measurements (for free-free and synchrotron), as well as the CMB dipole.

A time series of signal data was generated by “scanning” the simulated sky according to the PSI and FIRE prescriptions, to which was added a simulated time series of noise. This time stream was binned into the pixel on the sky corresponding to the spacecraft attitude. The noise time stream was generated in runs of length corresponding to $\simeq 2 \times 10^6$ pixels. Since each great circle contains $\sim 6 \times 10^3$ pixels, this allowed us to wrap 60 (30) times on each scan circle for PSI (FIRE), and cover 6 adjacent scan circles with correlated noise. For FIRE we simulated the actual number of rotations per great circle, while for PSI we stopped for practicality at $N = 60$. As can be seen in Fig. 2, we are approaching the asymptotic regime at this N , as varying the number of rotations in the simulations confirmed. By choosing $N = 60$ we were able to obtain coherence in the simulated time stream over several great circles in the sky to maximize our sensitivity to striping. Lower resolution simulations with even more correlated great circles showed no extra cross-scan striping.

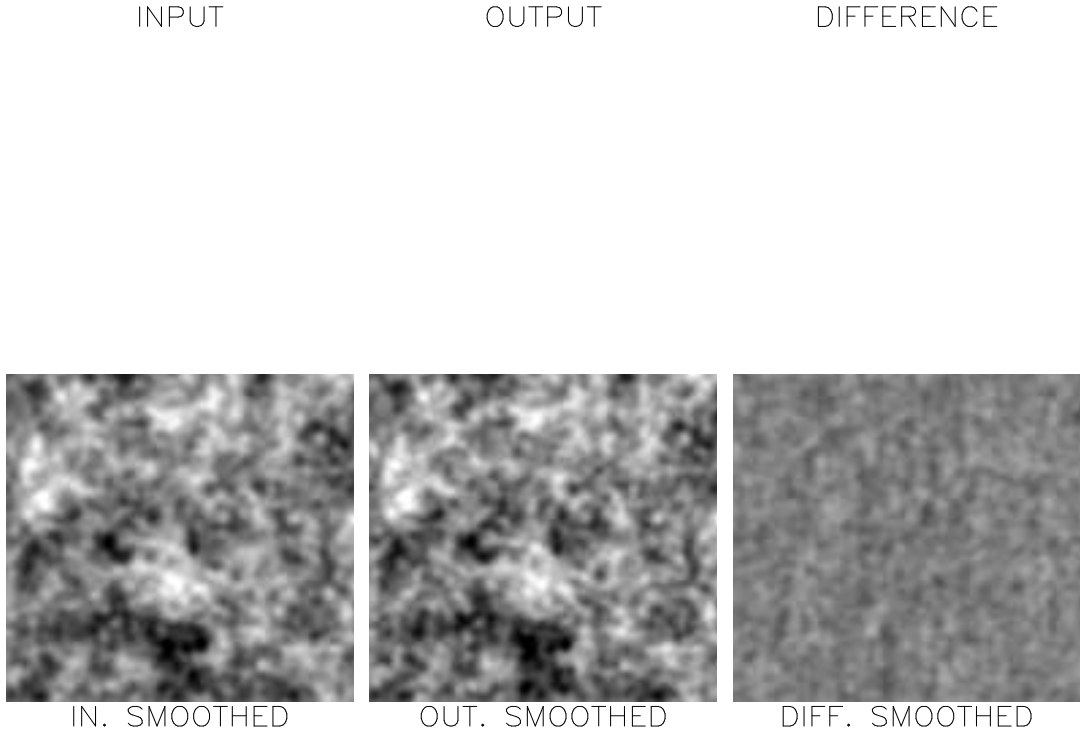


Fig. 5a PSI simulation of a small patch, enlarged for clarity. Same as Figure 4, for a $14^\circ \times 14^\circ$ equatorial region (where sensitivity and the possible effects of $1/f$ noise are worst). The pixel size is $3.6'$ (i.e. $3.5 \times$ oversampling). The saturation level has been set at $\pm 200 \mu\text{K}$ for this plot. The bottom row is smoothed to the $12.6'$ beam size. The scan direction is vertical. **Note:** Full 6 panel (8 k) version of this figure available at <http://astrophysics.jpl.nasa.gov/PSI/>.

For both PSI and FIRE, the power spectrum of the simulated noise was derived from real amplifier data. These data supported the assumption of a uniform random phase distribution for the simulated data, allowing us to generate the time streams in the simulation from the known power spectra. The noise added into the time stream was scaled relative to the signal map to the level expected *after* foreground removal from 2 years of observation. This level was determined in separate simulations (not described here) of foreground removal that used the raw instrumental noise levels (see Gaier et al. 1996a for 90 GHz performance) and beam sizes expected at each frequency (similar but preliminary studies are described in Brandt et al. 1995).

For PSI the data stream came from 44 GHz tone-stabilized HEMTs, sampled at 500 Hz for 500 s. We derived a power spectrum that was well-fitted by white noise plus $1/f$ noise with $f_{\text{knee}} = 10$ Hz. Similar measurements for FIRE bolometers gave a spectrum well-fitted by white noise plus $1/f$ noise with $f_{\text{knee}} = 0.03$ Hz.

The N rotations were averaged together to produce one great circle of data. Offsets between scan circles were removed simply by subtracting the mean on each circle. (For FIRE a gradient was also subtracted, to remove the small residual asymmetry shown in Figure 2 for $N = 30$. In practice this has essentially no effect on sky power, since the sky must “close” around the circle.) The result is shown in Figure 4, which looks identical at 600 dots per inch for either the PSI 90 GHz channel or the FIRE 100 GHz channel. Note that time domain drift removal in our configuration is easier than it was for *COBE*-DMR (e.g. Bennett et al. 1994), since we reference to the poles in every scan.

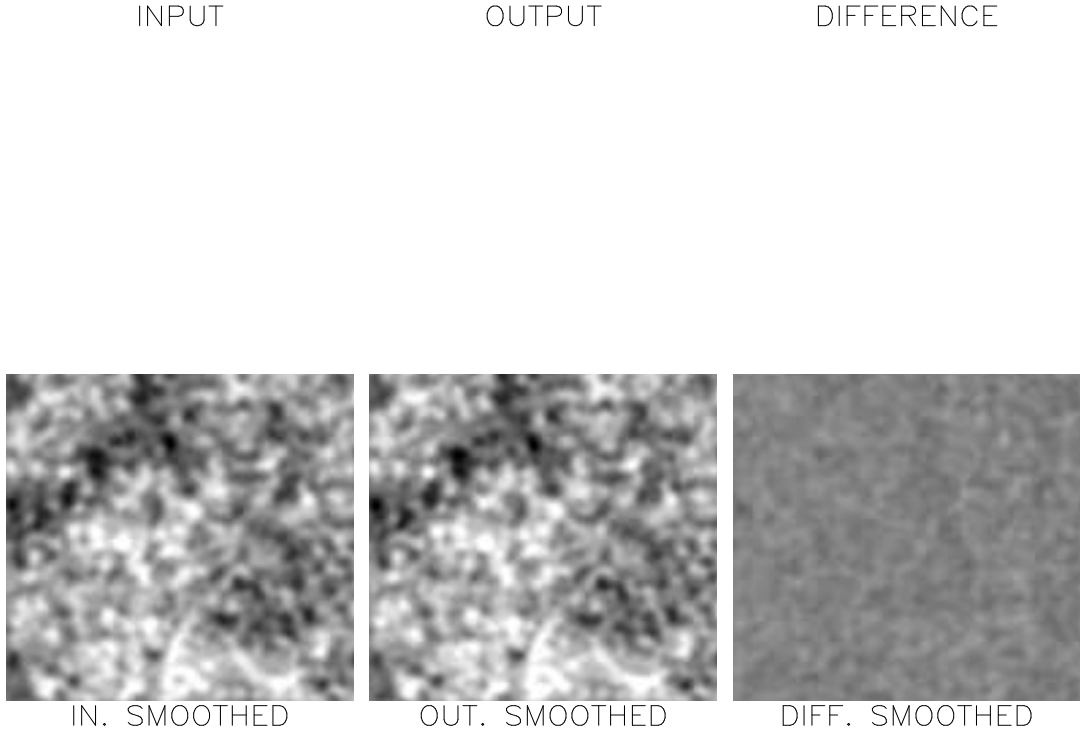


Fig. 5b FIRE simulation of a small patch, enlarged for clarity. Same as before, with a $10^\circ \times 10^\circ$ equatorial region. The pixel size here is 2.25×2.25 . The bottom row is smoothed to the 8' beam size. The scan direction is vertical. **Note:** full 6 panel (8k) version of this figure available at <http://astrophysics.jpl.nasa.gov/PSI/>.

Figure 5a shows a $14^\circ \times 14^\circ$ patch of sky for the PSI experiment enlarged for clarity to the

point that the printer can show a true gray scale. The beam size is 12'6 and the pixel size is 3'6, set by the sampling rate. The top row is shown at full pixel resolution; the bottom row is smoothed to the beam size. Left to right the panels show the assumed and observed skies, and the difference. The signal-to-noise ratio (SNR) is 1.1 even on the *pixel* scale. There are small residual “stripes” along scan lines (vertical here), exactly as expected from the theoretical calculations. An additional destriping step was performed for the PSI small patch simulations, where the mean of each scan across the patch was subtracted.

Figure 5b shows the same thing for the parameters of the FIRE experiment at 220 GHz, the highest frequency channel at which CMB fluctuations are likely to be usefully measured. The beam size is 8' and the pixels are 2'25, again set by the sampling rate. The patch plotted here is $10^\circ \times 10^\circ$, and the panels represent the same things as for the PSI figure, except that here the lower three panels have now been smoothed by 8'. The SNR achieved by PSI and FIRE will allow super-resolution, i.e., information can be extracted on angular scales substantially smaller than the beam size, and in practice one would make images that over-sample the beam by significantly larger factors than we have used here.

To quantify in a different way the effect of the residual striping along scan lines we have extracted the power spectrum of fluctuations from our simulated skies. Simulated full-sky images at the highest achievable resolution were observed with the PSI or FIRE strategy, including the effects of noise. From these we calculated the C_ℓ spectrum, where C_ℓ is the usual squared amplitude of the average spherical harmonic at multipole ℓ (see e.g., White, Scott & Silk 1994). Each input C_ℓ is one realization of the underlying average sky, and hence the power spectra show the effects of cosmic and sample variance at each multipole. We assumed for convenience that foregrounds had been removed over 80% of the sky with attendant increase in the noise level (see above). The other 20% of the sky (the Galactic plane) was ignored. In practice the fraction of the sky contaminated with foregrounds may be somewhat higher. The only effect of this would be a corresponding increase in sample variance.

Figure 6 shows the spectrum of multipole moments derived from our input, output, and difference images. Figure 6a is for a PSI simulation at 90 GHz, with the 12'6 beamsize. Figure 6b shows the same thing for FIRE, with a beam-size of 8'.

Each plot has two panels: the upper panel has $\ell(\ell+1)C_\ell$ on the vertical axis, so that the plot is power spectrum per logarithmic interval in ℓ ; the lower panel has C_ℓ on the vertical axis, this being the natural way to indicate noise, since pure white noise is then a horizontal line. The C_ℓ 's extracted from the input image are shown shifted vertically by two orders of magnitude to separate them from the output image C_ℓ 's. Note that both the input and output power spectra are the underlying theoretical spectra multiplied by the experimental window function, which is why they drop off faster at high ℓ than the more familiar theoretical curves. Also note that, as expected, the output power spectrum is the sum of the input and the noise spectra.

Four points are worth emphasizing: 1) no significant artifacts are apparent in the output sky power spectrum; 2) the difference image spectrum (i.e., the noise estimator) is nearly white noise over all angular scales, with some extra power at large scales where the SNR is largest; 3) the variance over the sky is σ_{\max}^2 , as expected; and 4) we expect to be able to determine the power spectrum efficiently and *without smoothing* out to $\ell \simeq 900$ (for PSI) and $\ell \simeq 1400$ (for FIRE).

These imaging simulations reinforce our analytic calculations. Not only are there no significant artifacts in the images, there is none in the power spectra either. The increase of the RMS noise over the pure white noise case is exactly as predicted by Eq. (22). Moreover, the simulations demonstrate that it is straightforward to analyze the time-stream data and produce a two-dimensional image of the sky. Many refinements of the method are possible, particularly concerning removal of offsets between scan circles, but even the simple method we used here works extremely well.

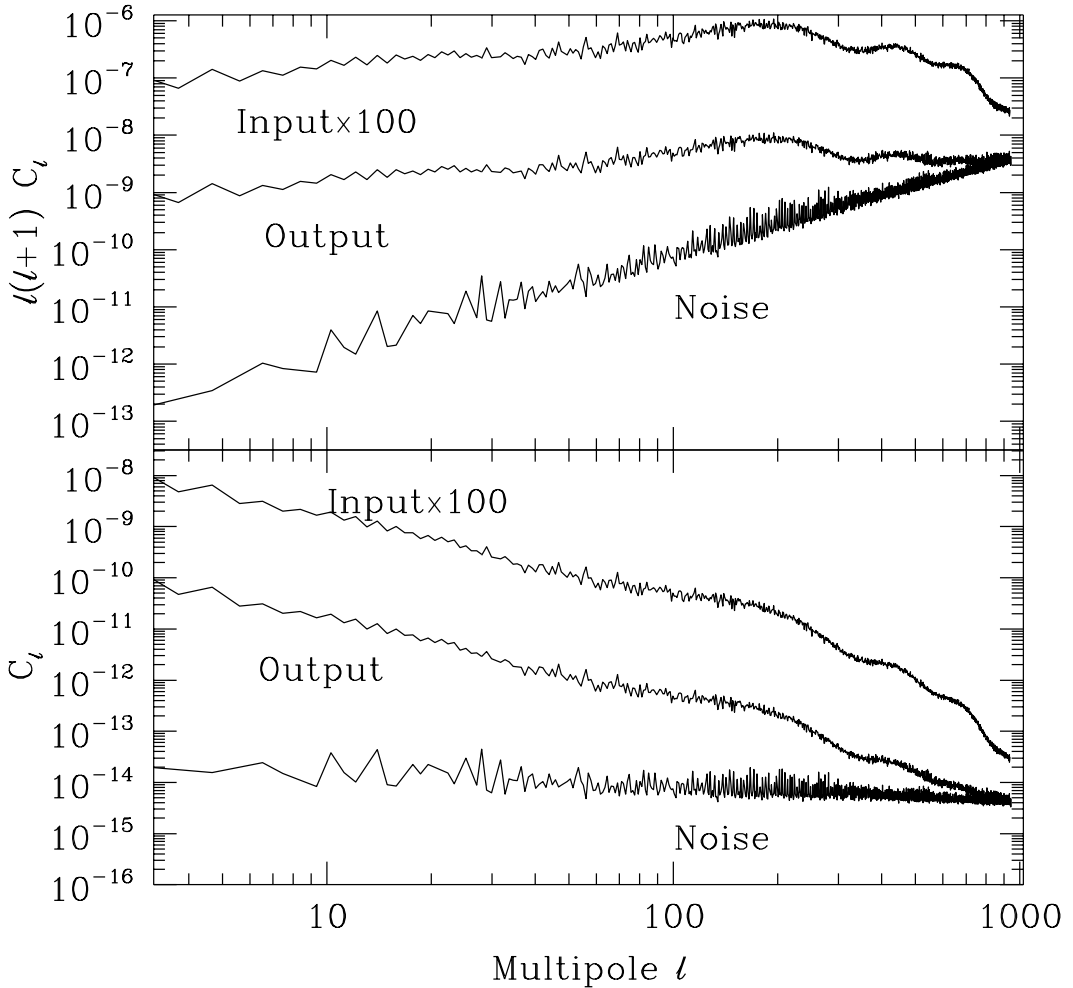


Fig. 6a PSI power spectra. The three curves plotted are from the input, output, and difference images. We took one realization of a standard CDM sky and observed it with the PSI spin-chopping scheme. The top curve is the power spectrum of the (noiseless) input data, shifted upward to avoid overlap. Note that the theoretical power spectrum has been convolved with the experimental beam. The jaggedness of this curve is just a reflection of the statistical nature of the model. The middle curve is the power spectrum fitted to the output image, equivalent to the lower left panel of Figure 4. *No smoothing has been applied in ℓ , i.e., every individual ℓ mode is calculated.* The bottom curve is the power spectrum of the difference image (i.e., output minus input), equivalent to the lower right panel of Figure 4. Here the beamsize was taken to be 12.6', with 3.6 pixels, and a noise level of $24 \mu\text{K}$ for a 12.6' resolution element. Note that the noise is close to white on all angular scales, and that it only dominates for $\ell \gtrsim 900$. **Top:** the familiar way of plotting power spectra, with $\ell(\ell+1)C_\ell$ on the vertical axis. **Bottom:** The same plot with C_ℓ on the vertical axis, so that pure white noise appears as a horizontal line.

4 CONCLUSIONS

PSI and FIRE image the sky in the most direct way possible, scanning it pixel by pixel. This

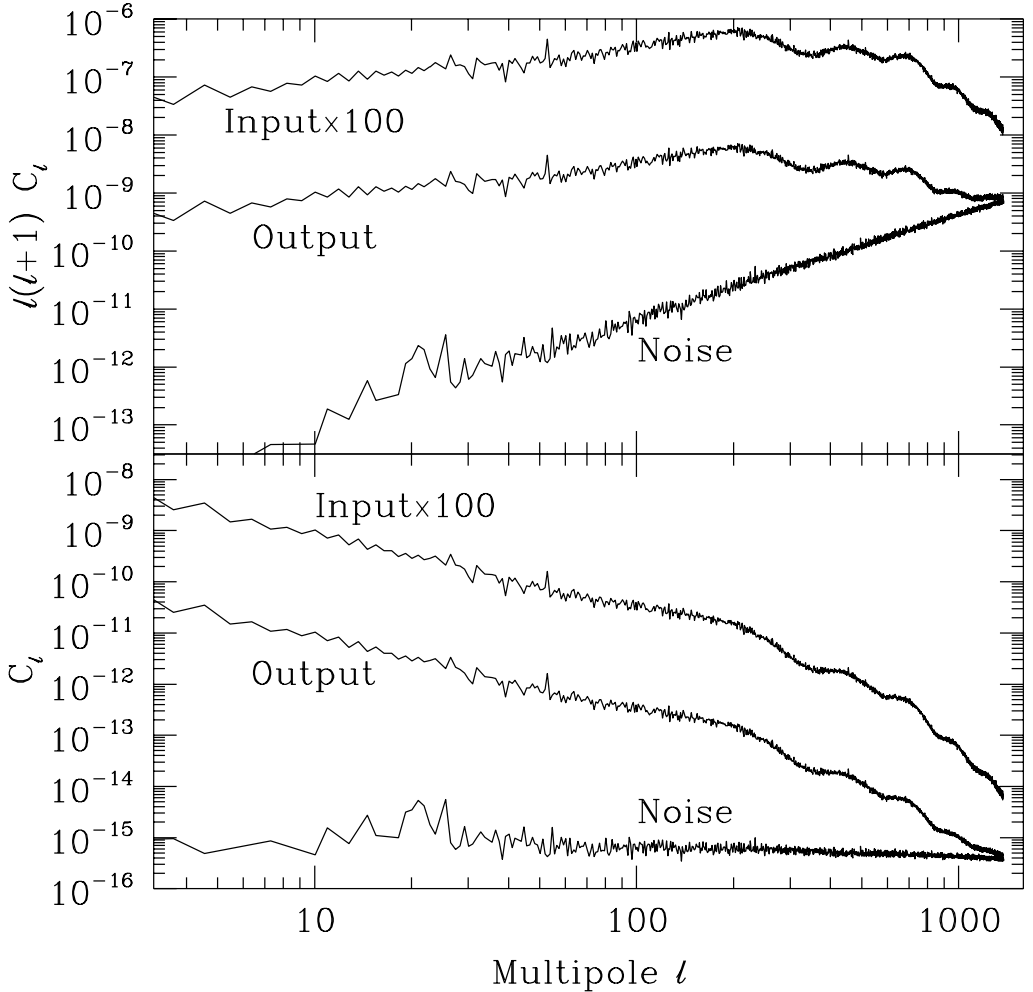


Fig. 6b FIRE power spectra. The same as Figure 6a, but for the parameters of the FIRE experiment. Here the beamsize was taken to be $8'$, with 2.25 pixels, and a noise level of $25 \mu\text{K}$ for an $8'$ resolution element. Note again that the noise is close to white on all angular scales, and that it only dominates for $\ell \gtrsim 1400$. **Top:** the familiar way of plotting power spectra, with $\ell(\ell+1)C_\ell$ on the vertical axis. **Bottom:** The same plot with C_ℓ on the vertical axis, so that pure white noise appears as a horizontal line.

strategy, enabled by a combination of technological advances in detectors, appropriate mission design, and favorable conditions at L_2 , has important technical and scientific advantages over that used by COBE-DMR, in which differences are measured between widely-spaced parts of the sky. The technical advantages include simplicity of the hardware and spacecraft operations, and benign and extremely stable thermal conditions with the Sun-pointed spin axis. The scientific advantages include high angular resolution, high sensitivity, and the independence of data from different parts of the sky. This last factor not only eliminates possible aliasing of signal from high foreground regions into low foreground regions and localizes the effects of transients, but also allows data to be analyzed as they are taken. The first slice of the sky can be seen at the first downlink and analyzed

immediately. Mission performance and systematic errors can be investigated almost immediately to microkelvin levels.

Laboratory measurements of the transistor amplifiers and bolometers used by PSI and FIRE respectively show that their noise characteristics can be modelled extremely well as a combination of white and $1/f$ noise. There are no long-term memory effects, such as those familiar from IRAS, that would result in persistent offsets after bright objects are crossed.

We have shown both analytically and with extensive simulations of our experimental procedure that $1/f$ fluctuations on timescales that cannot be completely removed by the spacecraft spin are transformed by that spin into a small increase in near-white noise that introduces *no significant systematic errors*. Moreover, we have shown that the naive expectation that f_{knee} must be much less than the spin frequency is far too restrictive. PSI and FIRE can thus realize all of the potential advantages, both scientific and technical, of the spin-chopping strategy.

Acknowledgements This paper presents the results of one phase of research conducted at the Jet Propulsion Laboratory, California Institute of Technology, under contract with the National Aeronautics and Space Administration. We would like to thank all the members of the teams that were responsible for the development of the PSI and FIRE mission concepts. UCSB acknowledges support from NASA grant NAGW-1062 and NSF grant AST 91-20005 from the Center for Particle Astrophysics. Further information about the PSI and FIRE missions can be found on the World Wide Web at these url's: <http://astrophysics.jpl.nasa.gov/PSI/> and <http://mpfntas.jpl.nasa.gov/shiba/fire/>.

References

Bennett, C. L., et al., 1994, *ApJ*, **436**, 423
 Boggess, N. W., et al., 1992, *ApJ*, **397**, 420
 Brandt, W. N., Lawrence, C. R., Readhead, A. C. S., Pakianathan, J. N. & Fiola, T. M. 1994, *ApJ*, **424**, 1
 Cheng, E. S. et al. 1995, *ApJ*, **456**, L71
 de Bernardis, P. et al. 1994, *ApJ*, **422**, L33
 Gaier, T. et al. 1996a, *IEEE-MTT*, submitted
 Gaier, T. et al. 1996b, in preparation
 Ganga K., Page, L., Cheng, E., & Meyer, S. 1994, *ApJ*, **432**, L15
 Gundersen, J. O. et al. 1995, *ApJ*, **443**, L57
 Hancock, S. et al. 1994, *Nature*, **367**, 333
 Janssen, M. A. & Gulkis, S., 1992, in *The Infrared and Submillimeter Sky after COBE*, ed. M. Signore & C. Dupraz, Kluwer, Dordrecht, p. 391
 Lineweaver, C. H. et al., 1994, *ApJ*, 436;452
 Netterfield, C. B. et al. 1995, *ApJ*, **445**, L69
 Piccirillo, L. et al. 1996, in preparation
 Ruhl, J. R. et al. 1995, *ApJ*, **453**, L1
 Seiffert, M. D. et al. 1996, in preparation

Smoot G. F., et al., 1992, *ApJ*, **396**, L1

Tanaka, S. T. et al. 1996, ApJ; submitted astro-ph/9512067

White, M., Scott, D. & Silk, J., 1994, *ARA&A*, **32**, 329

Wollack, E. J. et al. 1993, *ApJ*, **419**, L49

Wright, E. L., Hinshaw, G. & Bennett, C. L., 1995, preprint, astro-ph/9510102